Experimental investigation of G-HPC based sandwich walls incorporated with metallic tube core under contact explosion

[1]Pengcheng Yuan, [1*]Shenchun Xu, [1]Jian Liu, [3]Yu Su, [2]Jun Li, [1]Kefo Qu, [1]Cheng Liu, [2]*Chengqing Wu

[1]Protective Structures Centre, Guangzhou University, Guangzhou 510006, China

[2]School of Civil and Environmental Engineering, University of Technology Sydney, NSW 2007, Australia

[3]RockTek Co. Ltd., Daye, 435106, China

Abstract: A novel geopolymer based high performance concrete (G-HPC) sandwich wall consisting of two G-HPC layers separated by a metallic tube core possessing high strength and lightweight structure was developed in this study. The contact blast tests with 1 kg TNT were subsequently conducted to explore the blast resistance of the developed sandwich walls. For this purpose, three sandwich walls and a C40 reinforced concrete (RC) slab were employed. The superior blast resistance of the sandwich walls was verified based on the experimental results as compared to the RC slab. The sandwich wall with a circular steel tube core exhibited a superior blast resistance than the wall with a circular aluminum alloy tube core, whereas the sandwich wall with a rectangular steel tube core revealed the best performance. The blast resistance and damage mechanism of the sandwich walls were subsequently analyzed. The accuracy of the available empirical formulas was also examined for predicting the damage in the sandwich walls under contact explosion conditions.

Keywords: Sandwich wall; Metallic tube core; Contact explosion; Empirical formulas

1. Introduction

The blast loading can cause a catastrophic damage, including the collapse of the buildings, massive loss of property and human lives, etc. [1]. To mitigate the blast effects on the structures as well as protect the property and ensure the safety of the inhabitants, the studies on the blast resistance of the buildings have received a worldwide attention in the recent years. As a typical protective structure, a solid anti-blast wall is generally designed to provide a reliable protection of the structures against the blast loading. However, a majority of the solid anti-blast walls are endowed with significant volume and mass to provide the blast resistance, which makes the fabrication and installation challenging. Thus, it is vital to develop the novel anti-blast walls with lightweight structure and superior strength.

A number of studies have been conducted to explore the anti-blast walls, such as the concrete masonry [2], concrete [3], steel-sandstone-steel [4], reinforced soil [5], temporary soil-filled [6] and wood-sand-wood [7] walls. Wang *et al.* [8] investigated the dynamic response of the polymer-retrofitted masonry walls subjected to a contact explosion. The authors reported that the polyurea layer effectively reduced the fragmentation of the walls. Alsayed *et al.* [9] evaluated the performance of the glass fiber-reinforced polymer strengthened infill unreinforced masonry walls against the blast loading. It was reported that the walls provided a low to moderate level resistance against the blast loading. Chen *et al*. [10] explored the blast mitigation mechanism of the water barriers under blast loading. It was demonstrated that the water barriers effectively provided an optimal blast wave mitigation effect. Hussein *et al.* [7] performed the open-space explosion tests on the wood-sand-wood wall, which was observed to effectively mitigate the blast wave energy. However, the solid anti-blast walls have been generally designed to be either very heavy or bulky to minimize the structural damage caused by the blast loading, thus, preventing their use in the urban areas with the constrained living spaces.

On the other hand, the composite material retrofitting techniques have been employed to enhance the blast resistance of the RC slabs [11-13]. The composite material retrofitted RC slabs have been reported to demonstrate a superior blast resistance. In addition, the steel-concrete composite slabs composed of the steel plates and concrete have been widely employed for protecting the structures. A number of studies have investigated the dynamic response of the steel-concrete composite slabs subject to the impact/blast loading [14-16]. The slabs were reported to exhibit superior blast and impact resistance as well as energy absorption capacity [15, 17, 18]. As compared to the RC slabs, the steel-concrete composite slabs could be designed to be thinner, thus, reducing the weight and volume of the protective members to a certain extent. Hence, the steel-concrete composite structures exhibit the advantages of the lightweight structure and superior blast resistance, which are more suitable for the urban areas.

In contrast with the steel-concrete composite structure, novel sandwich walls composed of two concrete layers separated by a metallic tube core (MTC) have been reported in this study (0). MTC consisted of two steel plates and metallic tubes connected by using the epoxy resin adhesive and blind rivets. The MTC and concrete layer were connected by using shear connectors. Conventional concrete is not considered in the present composite design. Brittle nature of the conventional concrete leads to massive cratering under severe blast loads in the contact detonation. The manufacturing of the conventional concrete also consumes significant natural resources and generates high carbon dioxide emissions [19]. New construction materials with low environmental pollution and high mechanical properties are deemed necessary to enhance the blast-resistant capacity of the engineering structures and protect the natural environment.

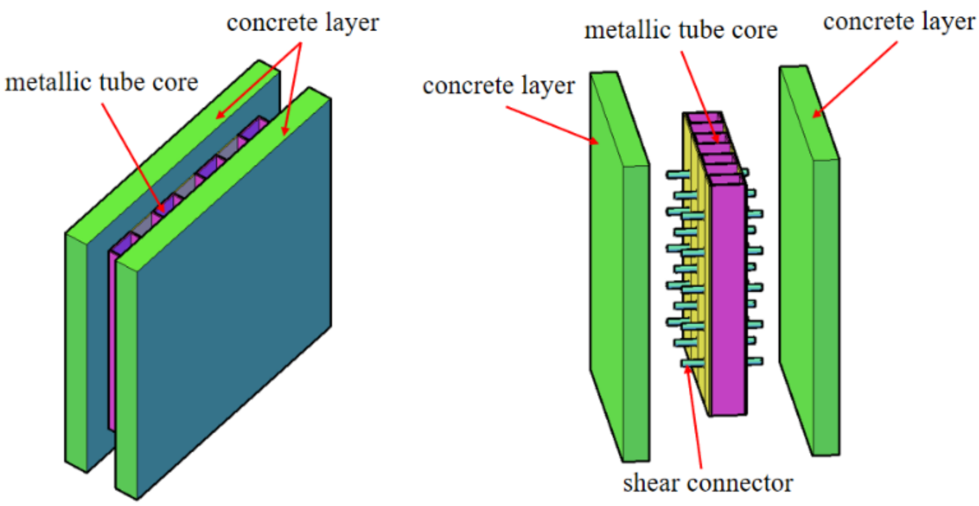

Fig. 1. Schematic of the sandwich wall

As the third-generation concrete [20], the geopolymer concrete (GPC) can reduce 40%-60% carbon dioxide emission as compared to the Portland cement concrete [21]. A number of studies have investigated the mix proportion and mechanical properties of GPC [22-25]. It has been commonly reported that GPC possesses high mechanical properties [26], good durability [27] and excellent fire resistance [28]. Therefore, GPC was selected in this study to fabricate the proposed sandwich walls.

Similar to the conventional concrete, pristine GPC exhibits brittle characteristics under the static and dynamic loads [29]. To improve the toughness of GPC, the fibrous materials are usually incorporated in GPC [30, 31]. Meng *et al.* [32] studied the flexural and compressive strength of the steel fibre reinforced GPC material. As compared with the pristine GPC material, the flexural strength of the steel fibre reinforced GPC was significantly improved from 4.24 MPa to 15.06 MPa, and the compressive strength was also enhanced. Khan *et al.* [33] reported that 2% volumetric ratio of the steel fibres could enhance the compressive strength of GPC by 18%. The steel wire mesh (SWM) reinforcement also represents an effective approach to enhance the concrete ductility. SWM has been reported to effectively mitigate the perforation and spalling of concrete under blast loading [26]. Li *et al.* [34, 35] investigated the performance of the SWM reinforced concrete slabs under blast loading. It was observed that the SWM reinforcement effectively enhanced the blast resistance of the concrete slabs through bridging effect and localized membrane effect. Therefore, SWM was incorporated in GPC in this study to enhance its toughness as well as to further improve the blast resistance of the structural members.

In this study, the blast resistance and failure modes of G-HPC sandwich walls with MTC interlayer were analyzed against the contact explosions, and comparison was made against a normal strength concrete slab. The spalling and crater areas of the walls/slab were quantitatively analyzed and compared. The damaged sandwich walls were cut to observe the deformation of the metallic tube core. The feasibility of utilizing the literature reported analytical and empirical methods to predict the sandwich wall damage under blast loading was also evaluated. The findings obtained in this study provide a reference for the protective design of such type of walls under contact explosions.

2. Design of G-HPC sandwich walls

The anti-blast concrete walls have been generally designed to be either heavy or bulky to minimize the structural damage caused by the blast loading, thus, it has the disadvantages of inconvenient construction and limited use area. In order to surmount the disadvantages of the anti-blast concrete walls and improve its blast resistance, a novel lightweight sandwich wall was designed. As illustrated in Fig. 2, the sandwich wall composed of two SWM referenced G-HPC layers separated by a metallic tube core (MTC). MTC consisted of two steel plates and metallic tubes connected by using the epoxy resin adhesive and blind rivets. The MTC and concrete layer were connected by using shear connectors. When subjected to contact explosion, an intense blast wave directly impacted on the top G-HPC layer. The top G-HPC layer with high compressive strength was designed to resist the intense blast wave and dissipate partial blast wave energy. After that, the blast wave reached the MTC layer and further dissipate partial blast wave energy owing to the large deformation of the MTC layer. At the same time, numerous fragments generated by the top G-HPC layer were intercepted by the MTC layer with high ductility and strength, thus, mitigating the damages to the occupants and equipment owing to the high-speed fragments. The SWM reinforced G-HPC on the bottom layer was designed to further absorb the blast wave energy, and utilizing the SWM to mitigate the high-speed fragments. Meanwhile, the bottom G-HPC layer can provide resistance for the deformation of MTC layer.

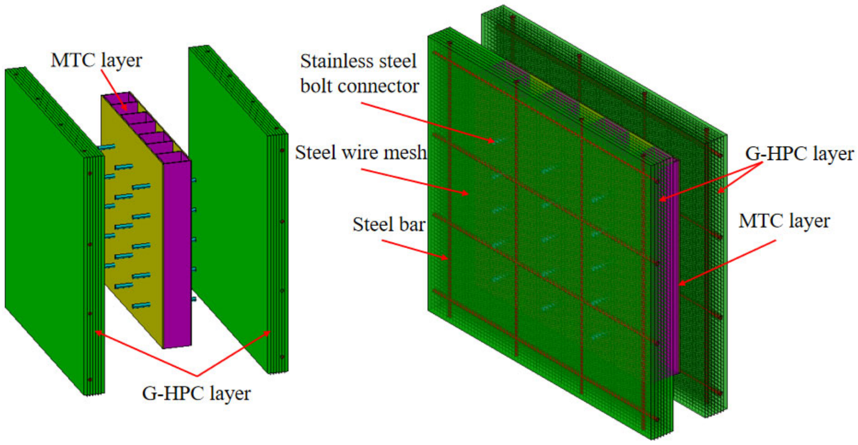

Fig. 2. 3-D view of the sandwich walls

Three G-HPC sandwich walls containing different MTCs (named as SPS-1, SPS-2 and SPSA-2, respectively) were prepared. The SPS-1 and SPS-2 walls were designed with the rectangular and circular steel tubes, respectively, whereas the SPSA-2 wall was designed with the circular aluminum alloy tubes. All sandwich walls were of cuboid shape with dimensions 1500 mm × 1500 mm × 200 mm. The details are shown in Fig. 3.

For the SWM reinforced G-HPC layers, the dimensions and construction of the SWM reinforced G-HPC layers of three sandwich walls are the same. The steel bars with 8 mm diameter were placed 460 mm apart on the G-HPC layers. And six layers of SWM with dimensions 1400 mm × 1400 mm (length and width) were also reinforced in the G-HPC layers. The concrete cover of the steel bar of the G-HPC layers was 20 mm, and two layers of SWM were placed on the concrete cover. Correspondingly, the remaining four layers of SWM were evenly placed on the G-HPC.

For the MTC layer, MTC contained two steel plates, nine metallic tubes and thirty stainless-steel bolt connectors. The dimensions of steel plate were 1250 mm × 1250 mm × 1 mm, whereas the metallic tubes had dimensions 1250 mm × 80 mm × 1.2 mm (length × outside diameter × thickness). The stainless-steel bolt connectors were fixed on the steel plates, retaining the integration between MTC and G-HPC layer. Subsequently, the bottom/top steel plate and nine metallic tubes were bonded together using the epoxy resin adhesive. The blind rivets with 3.2 mm diameter (GB/T 12618.1-2006) [39] were employed to further strengthen the connection between the steel plates and metallic tubes. Expanded polystyrene (EPS) was used around MTC to separate the top and bottom G-HPC layers, as the dimensions of MTC were smaller than the G-HPC layers.

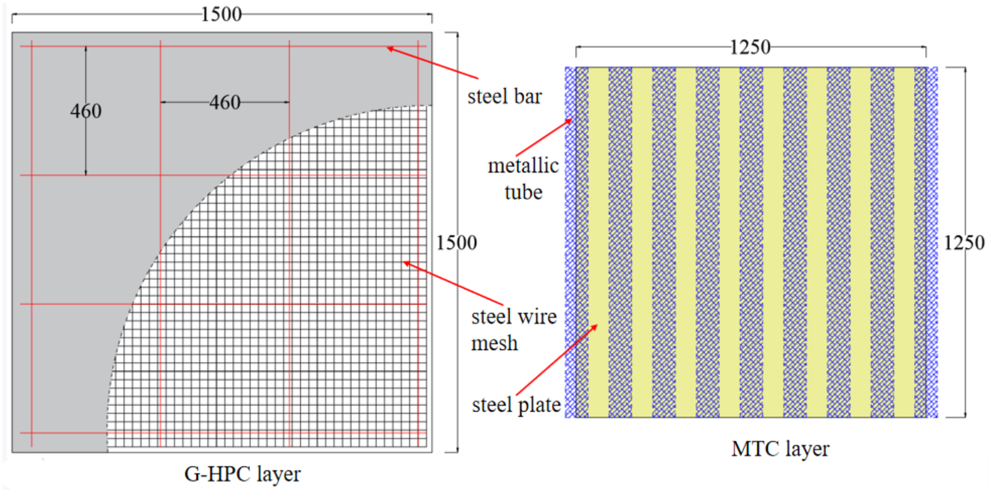

(a) The plan views of the sandwich walls

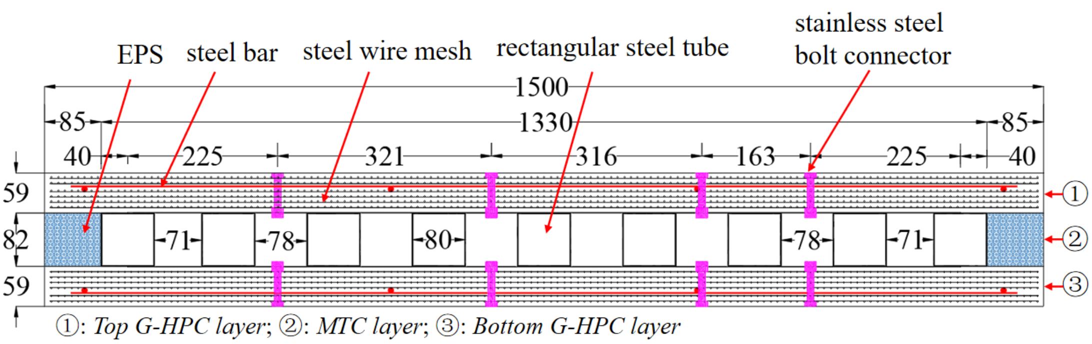

(b) The cross-section of the SPS-1 wall

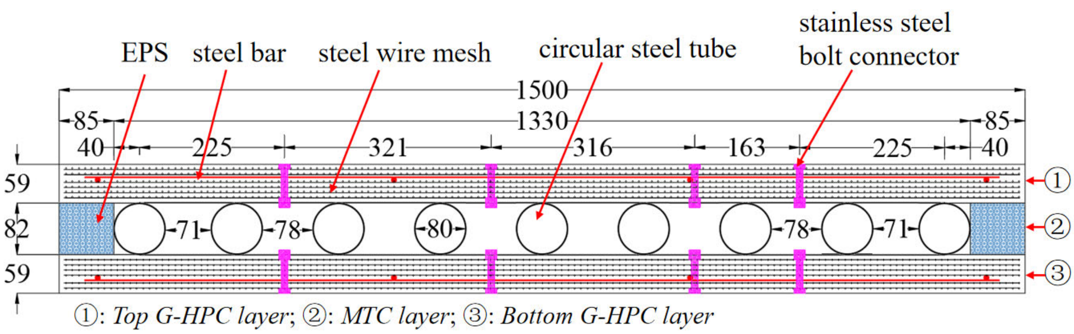

(c) The cross-section of the SPS-2 wall

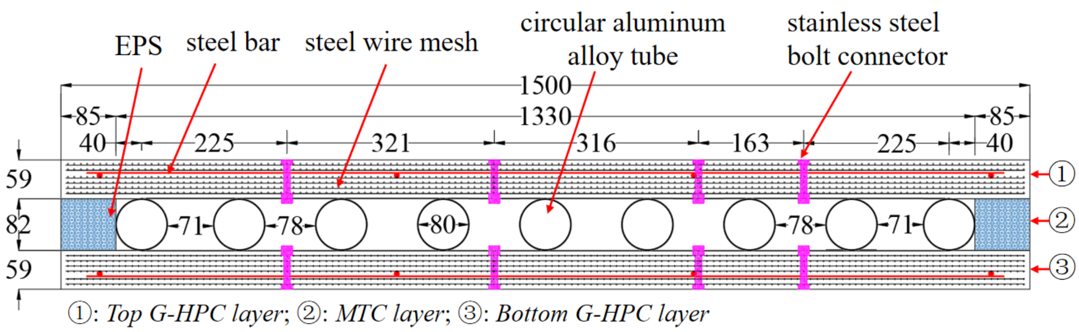

(d) The cross-section of the SPSA-2 wall

Fig. 3. The details of the sandwich walls (Unit: mm).

3. Experimental Setup

3.1 Test design

In order to investigate the blast resistance and failure modes of the G-HPC sandwich walls with MTC interlayer against the contact explosions, three G-HPC sandwich walls containing different MTCs was designed and fabricated. The SPS-1 and SPS-2 walls were designed to explore the effect of steel tube shape on blast resistance of the sandwich walls. Thus, the rectangular and circular steel tubes were employed for SPS-1 and SPS-2 walls, respectively. To compare the influence of different metallic tubes materials on the blast resistance of the sandwich walls, the SPSA-2 wall was designed with the circular aluminum alloy tubes to compare the blast resistance with SPS-2 wall. In addition, the RC slab was designed as a reference to illustrate the blast resistance of the sandwich walls, which has the same dimensions (1500 mm × 1500 mm × 200 mm) as the sandwich walls. The RC slab was reinforced in two major directions with 16 mm rebar at a spacing of 200 mm (1.35% reinforcement ratio). The details of the RC slab are shown in Fig. 4, and the test design is presented in Table 1.

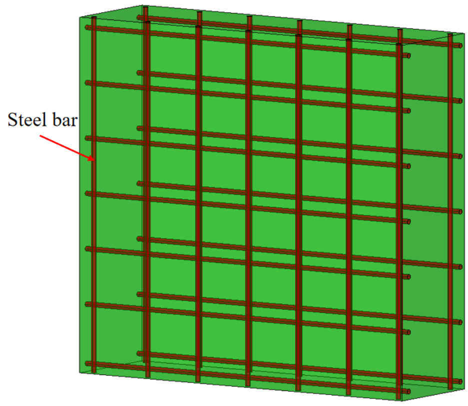

(a) 3-D view

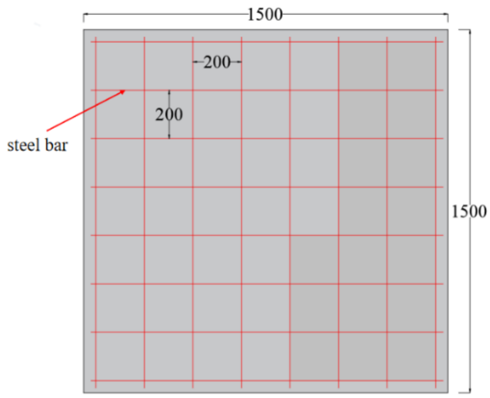

(b) The plan view

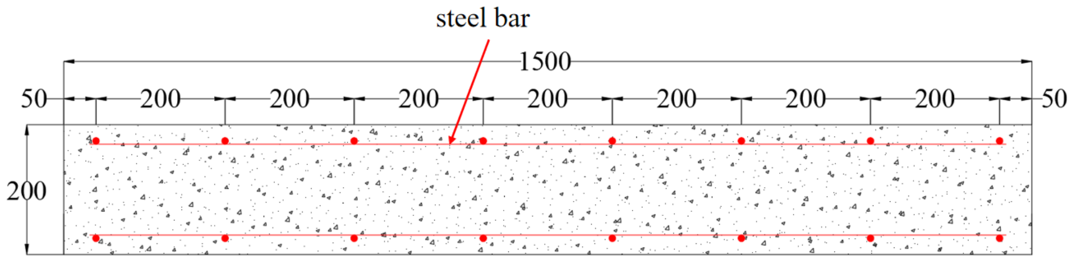

(c) The cross-section of the RC slab

Fig. 4. The details of the RC slab (Unit: mm).

Table 1 The test matrix

Slab	T_t (mm)	T_f (mm)	T_c (mm)	T_r (mm)	M_e (kg)
RC	200	NA	NA	NA	1.0
SPS-1	200	59	82	59	1.0
SPS-2	200	59	82	59	1.0
SPSA-2	200	59	82	59	1.0

**Note: T_t is the total thickness; T_f is the top G-HPC layer thickness; T_c is the MTC thickness; T_r is the bottom G-HPC layer thickness; and M_e is the TNT explosive charge.*

3.2 Materials

Three cubic G-HPC specimens with dimensions 100 mm × 100 mm × 100 mm and three cubic C40 concrete specimens with dimensions 150 mm × 150 mm × 150 mm were tested for uniaxial compression. The Chinese Standard GB/T 50081-2002 was employed to test the mechanical properties of G-HPC and C40 specimens. The typical stress-strain curves are shown in Fig. 5. The average compressive strength values of G-HPC and C40 concrete were determined to be 83 MPa and 38 MPa, respectively.

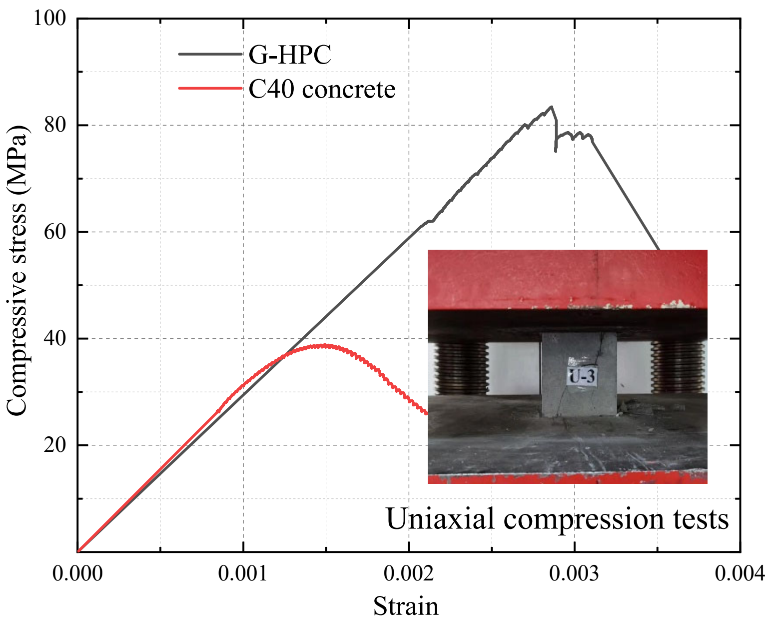

Fig. 5. The stress-strain curves of G-HPC and C40 concrete

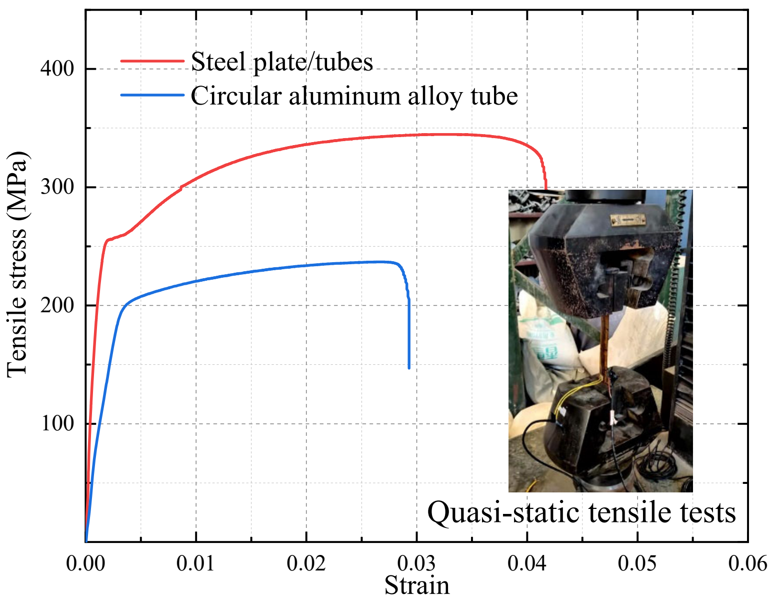

Fig. 6. The tensile stress-strain curves

HRB 400 steel bars with 8 mm and 16 mm diameters were utilized in this study. The diameter of SWM was 1 mm, and the mesh grid size was 10 mm × 10 mm. The steel plates and tubes of MTC were made of Q235B (GBT3091-2015) [36]. The circular aluminum alloy tubes comprised of 6063 T5 aluminum alloy (GB/T6892-2015) [37]. The Chinese Standard GB/T228.1-2010 was employed to test the tensile stress of the metallic materials. Fig. 6Fig. 6 presents the tensile stress vs. strain curves of the metallic materials. The M1O stainless-steel bolt connectors (GB/T 3098.6-2014) [38] in MTC had a 10 mm diameter and were made of 304 steel. The properties of the metallic materials are presented in Table 2.

Table 2 The properties of the metallic materials

Parameters	Grade	ρ (kg/m^3)	E (MPa)	f_y (MPa)	f_t (MPa)
Steel bar	HRB 400	7800	2.08×10^5	428.3	615.8
Steel plate/tubes	Q235	7800	2.05×10^5	255	344
Circular aluminum alloy tube	6063 T5	2700	6.90×10^4	193	236
SWM	--	7800	2.05×10^5	600	1200
Stainless-steel bolt connectors	304	7900	1.99×10^5	310	740

**Note: ρ is the density; E is the elastic modulus; f_y is the yield strength; and f_t is tensile strength.*

3.3 Specimen preparation

Fig. 7 shows the fabrication process of the RC slab, which included: (1) binding reinforcement with steel wires; (2) placement of the reinforcement; (3) casting the concrete; (4) curing the slab with the cover of coatings at a constant ambient temperature of 20 ± 5 °C for seven days.

(a) Fabrication of reinforcement (b) Casting the concrete

Fig. 7. The fabrication of the RC slab

The fabrication process of the SPS-1, SPS-2 and SPSA-2 walls was identical (Fig. 8), which included: (1) fabrication of MTC; (2) casting of the bottom G-HPC layers reinforced with six tiers of SWM and one-layer steel bar to attain a thickness of 59 mm (predicted); (3) placement of the metallic steel tube core; and (4) repeating (2) to fabricate the top G-HPC layer; (5) curing the walls with the cover of coatings at a constant ambient temperature of 25 ± 5 °C for 24 h, then steam curing at a high temperature of 90 ± 5 °C for 48 h.

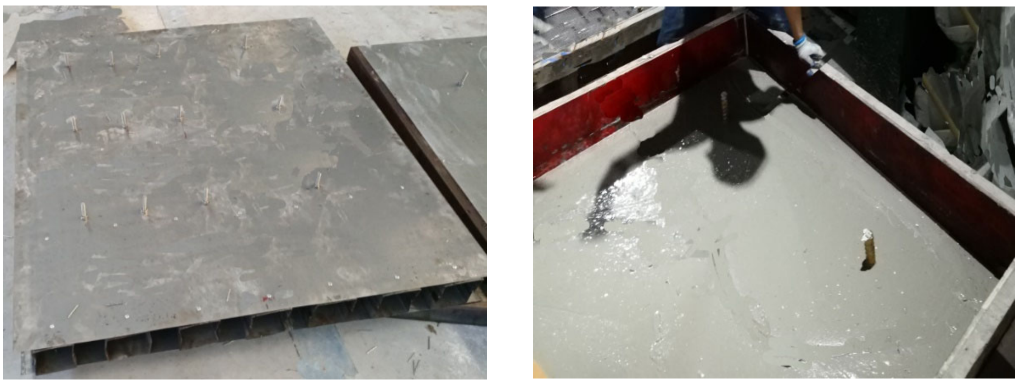

(a) Fabrication of MTC (b) Casting the bottom G-HPC layer

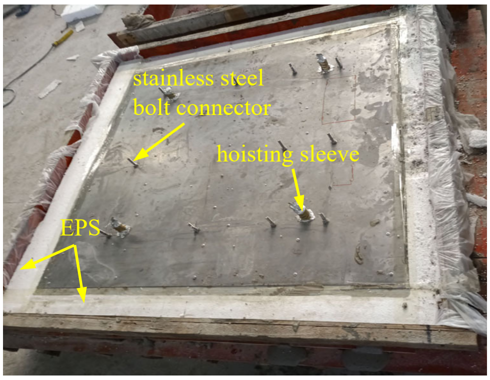

(c) Installation of EPS

(d) Installation of SWM and steel bar

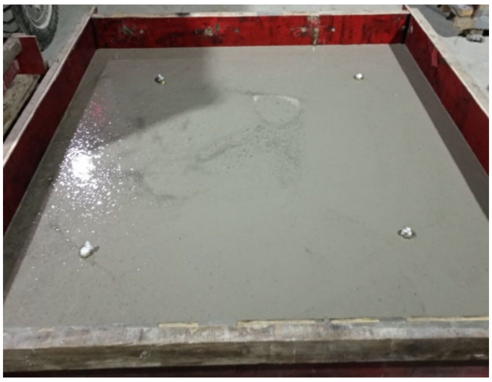

(e) Casting the top G-HPC layer

(f) Wall formation

Fig. 8. The fabrication of the sandwich walls

Fig. 9 shows the fabrication process of MTC, which included: (1) fixing the stainless-steel bolt connectors on the steel plates; (2) gluing the metallic tubes on the steel plates; and (3) strengthening MTC with blind rivets.

(a) Fixing the stainless-steel bolt connectors

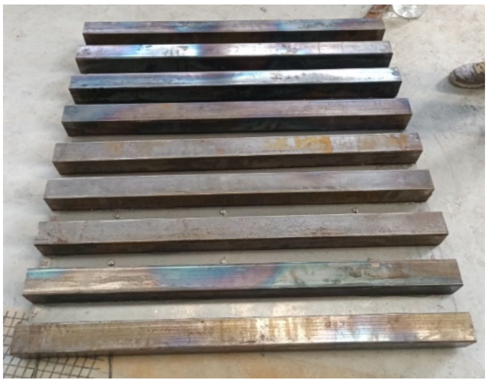

(b) Gluing the metallic tubes

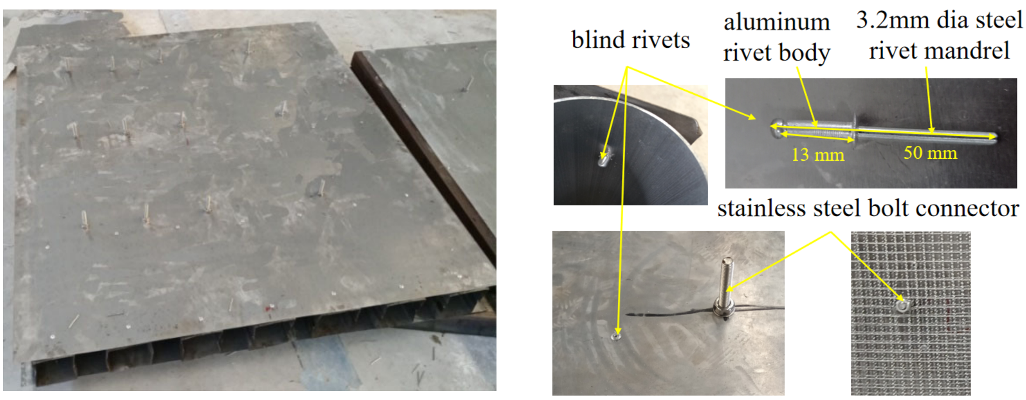

(c) Forming MTC (d) The details of the blind rivets

Fig. 9. The fabrication of MTC

3.4 Test setup

Fig. 10 presents the setup of the contact explosive tests. Four prismatic concrete piers of the same height were stamped on the ground. A square steel frame with a side length of 1500 mm was welded on the top of the concrete piers to provide a simple support to the slab. 1 kg TNT explosive (consisting of five 100 mm × 50 mm × 25 mm rectangular charges each with a mass of 0.2 kg TNT) was detonated at the center of the top surface of the wall. An electric detonator was inserted in the top rectangular charge to detonate the explosive.

Fig. 10. Test setup

4. Results

4.1 Summary of the Results

The damage to the concrete slabs under contact explosions is typically classified into three categories: crater, spalling and breach. As reported by Dua *et al.* [40], the breach failure further includes the perforation and punching failure modes. In this study, the perforation failure was further divided into three categories: perforation-spalling, perforation-critical and complete perforation (Fig. 11).

Fig. 11 (a) and (b) present the perforation-spalling mode where the top G-HPC layer presented a perforation, whereas a spalling failure was observed on the bottom G-HPC layer. Numerous G-HPC fragments were trapped by SWMs on the bottom G-HPC layer. Moreover, Fig. 11 (a) presents the MTC structure with a rectangular steel tube, whereas Fig. 11 (b) presents the MTC structure with a circular steel tube. Fig. 11 (c) shows the perforation-critical mode where a perforation was developed in the top G-HPC layer, with a critical perforation at the bottom G-HPC layer. The critical perforation observed on the bottom G-HPC layer referred to the minor fracture appearing on the bottom steel plate. In addition, SWMs were noted to be ruptured, and a number of fragments ejected from the bottom G-HPC layer. Fig. 11 (d) presents the complete perforation mode where an obvious hole was formed owing to the intersection of the crater and spalling.

Fig. 11 also presents the quantitative values of the measurement parameters, including crater diameter and depth as well as perforation and spalling diameter. Here, "d_c" refers to the crater diameter; "d_p" denotes the perforation diameter of the RC slab as well as the perforation diameter of the top G-HPC layer for the sandwich walls; "d_s" represents the spalling diameter; "d_{sp}" refers to the depressed deformation region diameter of the bottom steel plate; and "h_t" denotes the depth from the top surface to the metallic tube for the sandwich wall. "--" represented the missing data. The detailed test results are presented in Table 3.

Table 3 The experimental results

Specimen	d_c(mm)	d_p(mm)	d_s(mm)	d_{sp}(mm)	h_t(mm)	Failure mode
RC	551. 5	255.0	745.0	0	0	Complete perforation
SPS-1	395.0	240.0	597.5	385.0	185	Perforation-spalling
SPS-2	431.5	300.0	608.0	400.0	170	Perforation-spalling
SPSA-2	406.5	305.0	572.5	380.0	--	Perforation-critical

243

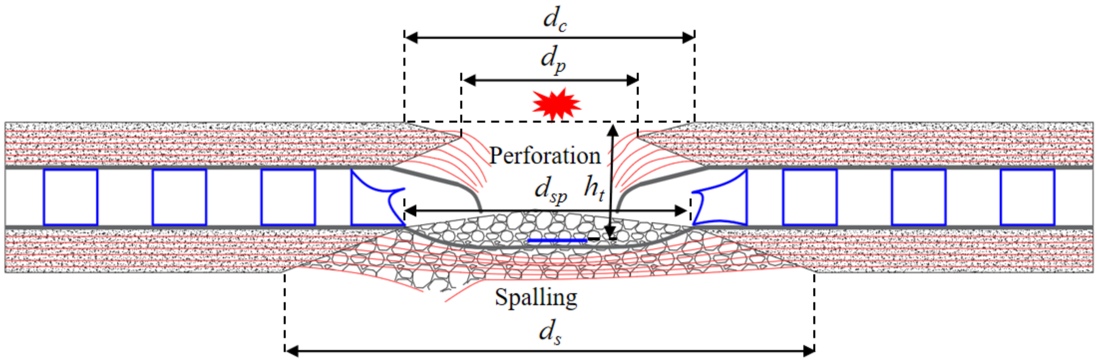

(a) The perforation-spalling mode of rectangular steel tube core

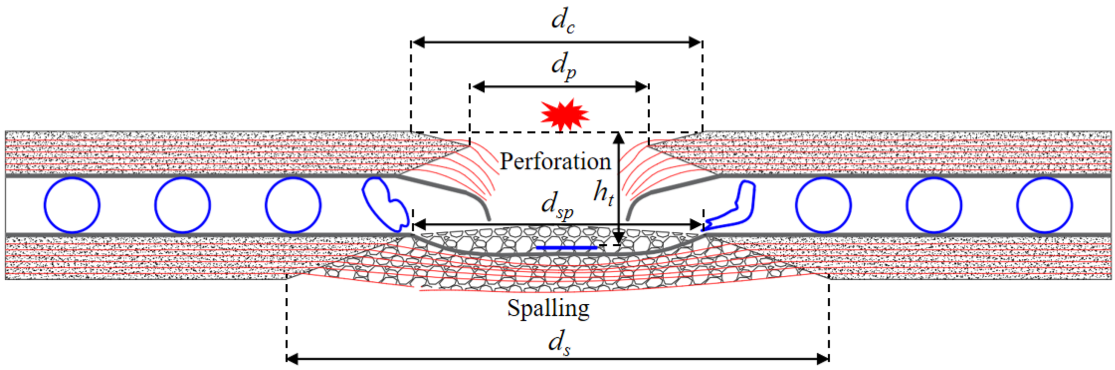

(b) The perforation-spalling mode of circular steel tube core

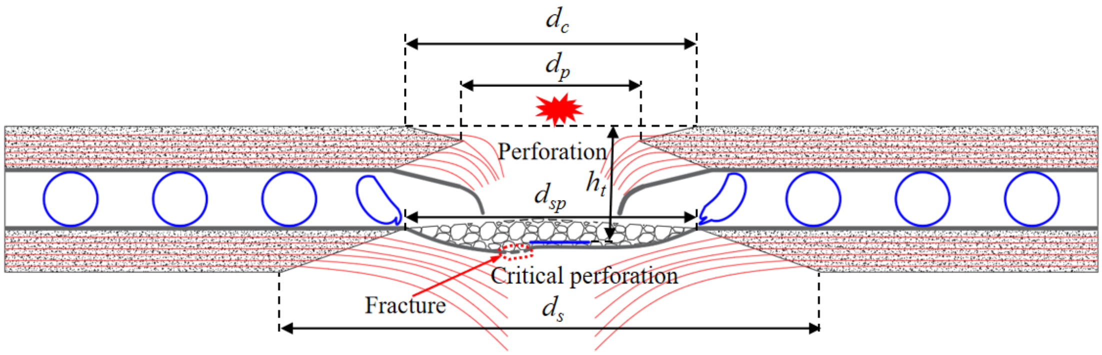

(c) The perforation-critical mode

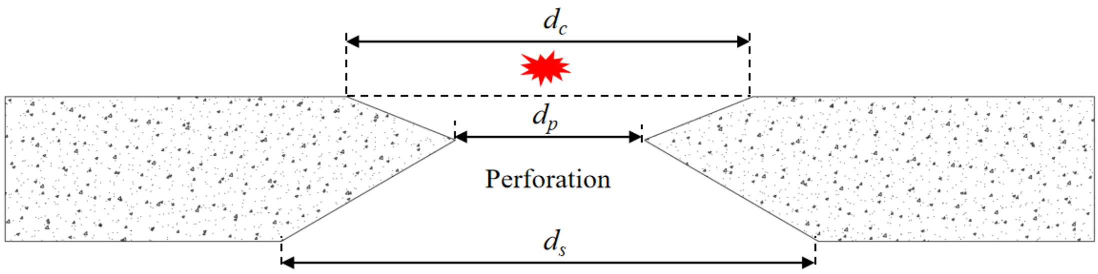

(d) The complete perforation mode

Fig. 11. The failure modes

4.2 Experimental observations

4.2.1 RC slab

Fig. 12 (a) and (b) present the typical perforation failure of the RC slab. The crater, perforation and spalling diameters were measured to be 551.5 mm, 255 mm and 745 mm, respectively. Correspondingly, the depths of the crater and spalling were 50 mm and 150 mm, respectively. The central steel bars exhibited deformation, and minor vertical cracks were observed on the side surface (Fig. 12 (c)).

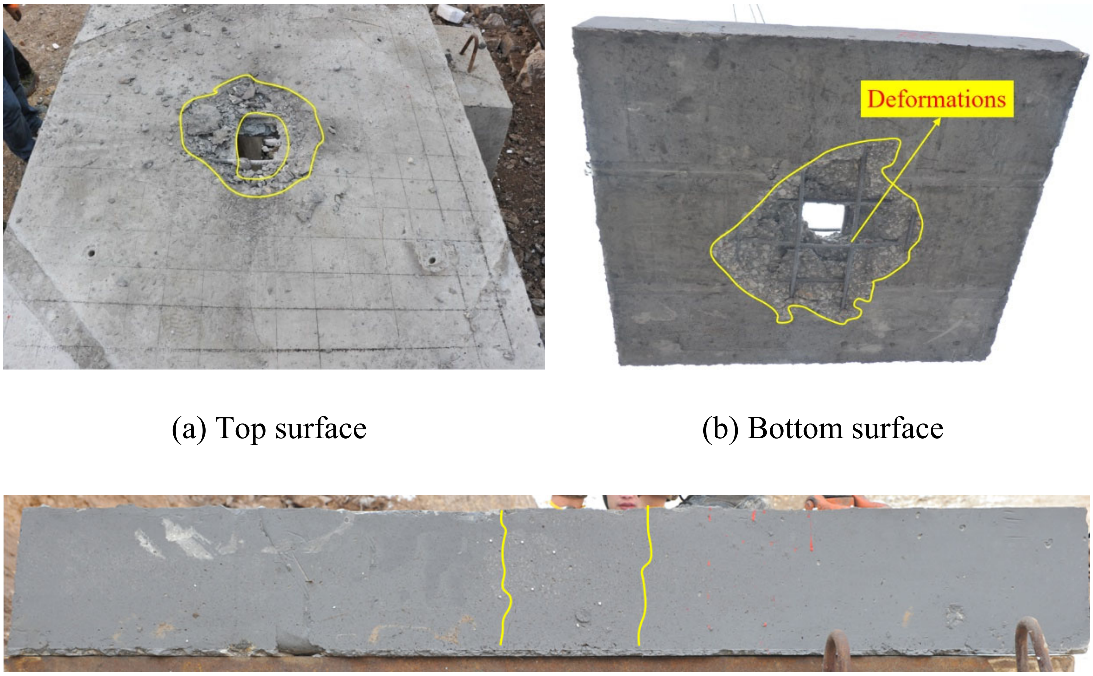

(a) Top surface (b) Bottom surface

(c) Side surface

Fig. 12. The RC slab

4.2.2 SPS-1 wall

Under 1.0 kg TNT (consisting of five 100 mm × 50 mm × 25 mm rectangular charges each with a mass of 0.2 kg TNT) contact explosion, an intense blast wave directly impacted on the top G-HPC layer of the SPS-1 wall, thus, the typical perforation failure was observed on the top G-HPC layer (Fig. 13 (a)). The crater and perforation diameter of the top G-HPC layer were determined to be 395 mm and 240 mm, respectively, whereas the corresponding depth from the top surface to the metallic tube was 185 mm. Furthermore, SWMs were noted to be ruptured and rolled inwards, with severe cracks observed along the edges of the top G-HPC layer. This may be owing to the following three reasons: (1) G-HPC near the edge of the top layer was not reinforced with SWMs (SWM dimensions were 1400 mm × 1400 mm), thus, reducing the ductility of G-HPC without SWMs reinforcement relative to the G-HPC layer. (2) The MTC layer (MTC dimensions were 1330 mm × 1330 mm) was enhanced the blast resistance of the top G-HPC layer than that without the MTC layer. (3) The blast waves propagating through the top G-HPC layer to the side surface and reflected as a tensile wave exceeded the dynamic tensile strength of G-HPC, hence cracking the top G-HPC layer. In addition, severe vertical cracks together with concrete spalling were observed on the side surface (Fig. 13 (c)).

For the blast wave propagating through MTC, the high compressive stress wave tore the top steel plate, along with flattening the fifth steel tube. Both fourth and sixth steel tubes were observed to slip and baroclinic deformation, which was caused by the diffusion of the blast waves. No obvious deformation was observed for the other steel tubes. As the compression stress wave continued to propagate downwards, the bottom steel plate and central G-HPC region on the bottom G-HPC layer produced large deformations, thus, leading to the generation of cracks in the central G-HPC region. The depressed deformation region diameter of the bottom steel plate was determined to be 385 mm (Fig. 13 (d)). In addition, a number of fragments from the top G-HPC layer were noted to be trapped through the bottom steel plate. From the middle cross-section (Fig. 13 (d)), the top surface of the bottom G-HPC layer benefitted from the strength and ductility of the bottom steel plate in resisting the blast wave, thus, preventing its surface from being crushed.

Once the blast wave reached the bottom surface, it was reflected and subsequently transformed into the tensile stress wave. After superposition of the reflected tensile and compression stress waves, the spalling damage was observed on the bottom G-HPC layer with a diameter of 597.5 mm, and the fragments of the concrete cover ejected from the wall. The central area of the G-HPC layer was noted to be severely crumbed. Numerous fragments were intercepted by SWMs, thus, mitigating the damages to the occupants and surroundings owing to the high-speed fragments. Several steel wires of the outermost SWM were also observed to be ruptured. In addition, the cracks on the bottom surface were also observed owing to the large tensile stresses, as shown in Fig. 13 (b).

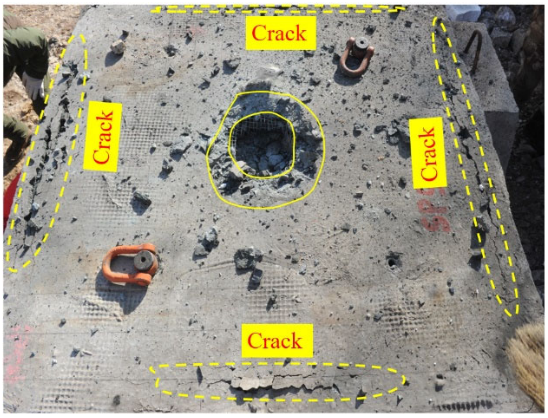

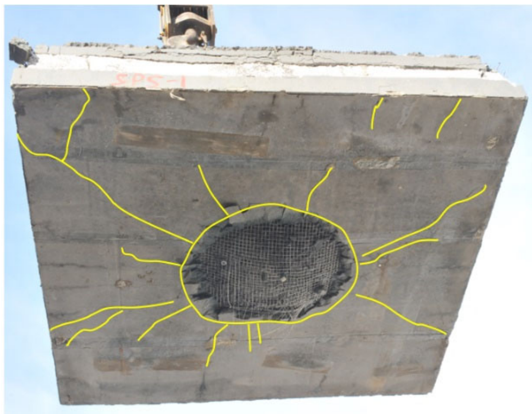

(a) Top surface (b) Bottom surface

(c) Side surface

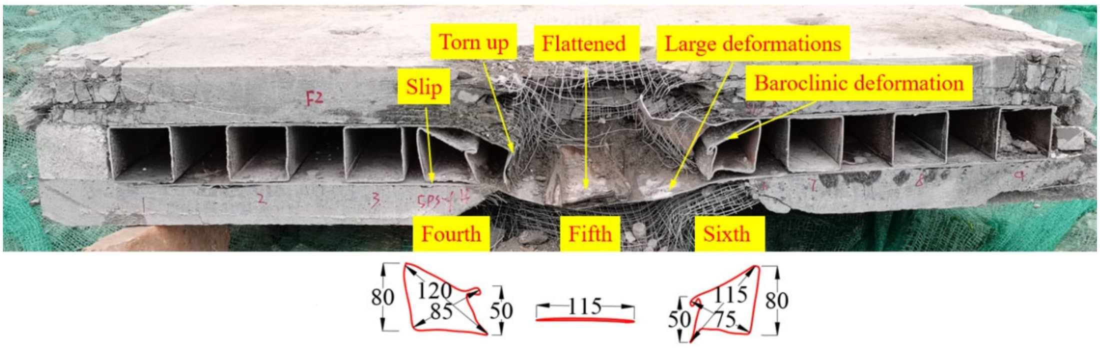

(d) Middle cross-section (mm)

Fig. 13. The SPS-1 wall

4.2.3 SPS-2 wall

The failure mode of the top G-HPC layer of the SPS-2 wall was similar to that of the SPS-1 wall. The crater and perforation diameters in the top G-HPC layer were measured to be 431.5 mm and 300 mm, respectively. The depth from the top surface to the metallic tube was 170 mm (Fig. 14 (a)). A small number of vertical cracks were observed on the side surface (Fig. 14 (c)), however, severe spalling was noted on the bottom G-HPC layer (Fig. 14 (b)).

The top steel plate of MTC was torn, however, the bottom steel plate demonstrated a large deformation without any tearing. The diameter of the depressed deformation region in the bottom steel plate was determined to be 400 mm. Further, a large number of fragments generated from the top G-HPC layer were prevented from ejection by the bottom steel plate.

Under the blast loading, the fifth tube was observed to be completely compacted with a width of 119 mm. The fourth and sixth tubes close to the detonation point experienced large elliptical deformations, with slips observed on both tubes. The other tubes exhibited no obvious deformation (Fig. 14 (d)).

The bottom G-HPC layer exhibited the spalling damage to the concrete cover with a diameter of 608 mm, whereas its central area crumbed severely (Fig. 14 (d)). Numerous fragments were observed to be trapped in SWMs, and several steel wires of the outermost SWM were fractured. Thus, SWMs were conductive in preventing the secondary injuries generated from the high velocity fragments. In addition, the radial cracks were observed at the bottom surface (Fig. 14 (b)).

(a) Top surface　　(b) Bottom surface

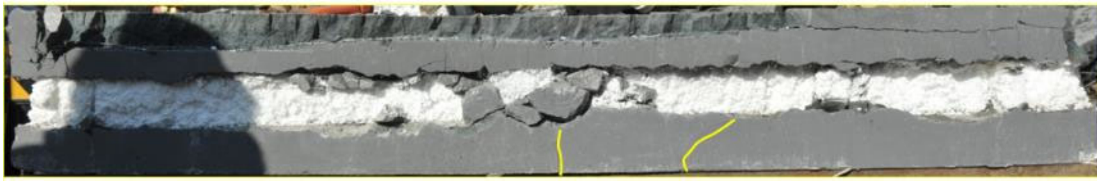

(c) Side surface

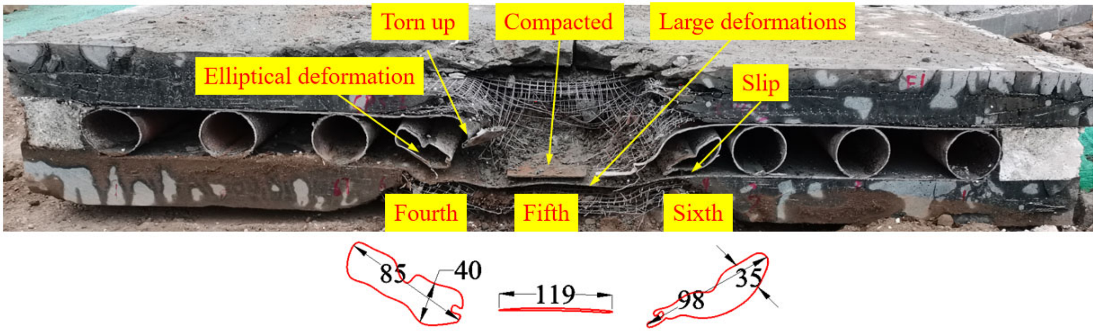

(d) Middle cross-section (mm)

Fig. 14. The SPS-2 wall

4.2.4 SPSA-2 wall

The failure mode (perforation failure and serious cracks along the edges) observed on the top G-HPC layer of the SPSA-2 wall is shown in Fig. 15 (a). The crater and perforation diameters of the top G-HPC layer were determined to be 406.5 mm and 305 mm, respectively. However, the depth from the top surface to the metallic tube was not measured as a small strip-shaped hole appeared on the bottom steel plate, and the critical penetration failure occurred at the bottom G-HPC layer. A few vertical cracks were also observed on the side surface (Fig. 15 (c)), and a small extent of spalling appeared on the top G-HPC layer as compared to the SPS-2 wall.

The top steel plate of MTC was observed to be torn. In contrast with the SPS-2 wall, a minor fracture occurred at the bottom steel plate, accompanied with a small strip-shaped hole. The depressed deformation region of the bottom steel plate was measured to be 380 mm. A few fragments from the top G-HPC layer were trapped by the bottom steel plate. The baroclinic deformation was observed between the sixth and fourth tubes. Further, a compaction appeared near the explosion side, and the slips were also observed in both tubes. The compaction and rupture occurred on the fifth tube, and the width of the compaction was determined to be 125 mm. Likewise, no obvious deformation was noted for the other tubes (Fig. 15 (d)).

The critical perforation failure of the bottom G-HPC layer was observed to take place, and the spalling diameter was 572.5 mm. The rupture was also noted to occur on SWMs. A large number of ejecting concrete fragments were produced, which represent significant danger for the occupants and surroundings. Additionally, the bottom surface exhibited numerous short radial cracks (Fig. 15 (b)).

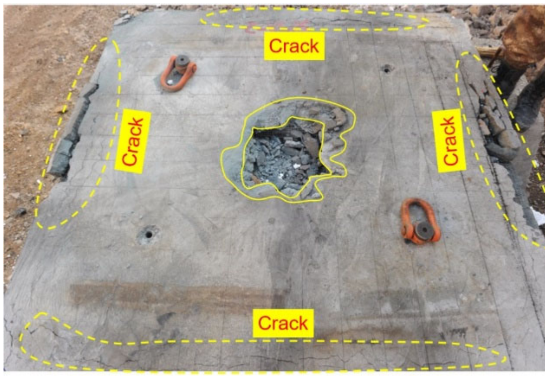

(a) Top surface

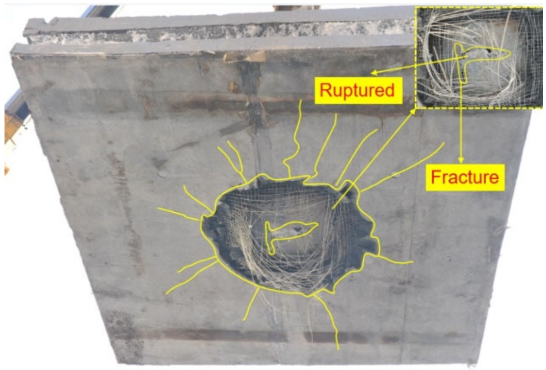

(b) Bottom surface

(c) Side surface

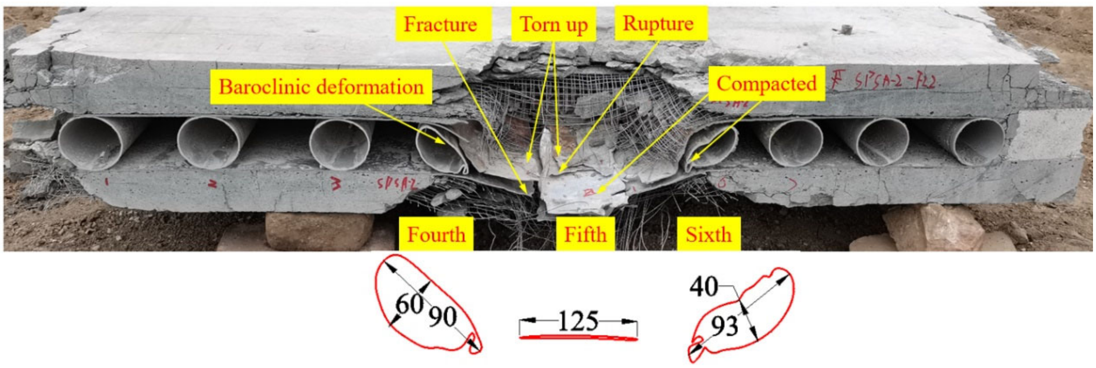

(d) Middle cross-section (mm)

Fig. 15. The SPSA-2 wall

4.3. Discussion

4.3.1 Diameters

The diameters of the crater (d_c), perforation (d_p), spalling (d_s) and depressed deformation regions of the bottom steel plates (d_{sp}) in the walls/slabs are shown in Fig. 16. The crater and spalling diameters of the RC slab were smaller than those of the sandwich walls, exhibiting a reduction up to 39.6% and 30.1%, respectively. The perforation diameter of the SPS-1 wall was smaller than that of the RC slab, whereas the perforation diameter of the SPS-2 and SPSA-2 walls increased by 17.6% and 19.6%, respectively. A minor difference was also observed in the diameters of the depressed deformation regions of the bottom steel plates of the sandwich walls.

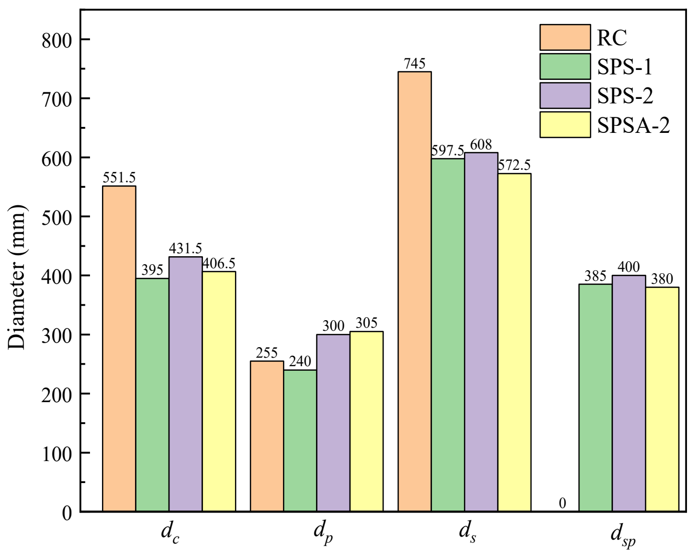

Fig. 16. The damage diameters

4.3.2 Failure mode analysis

Under 1.0 kg TNT (consisting of five 100 mm × 50 mm × 25 mm rectangular charges each with a mass of 0.2 kg TNT) contact explosion, the sandwich walls exhibited a superior blast resistance as compared to the RC slab. The damage of the sandwich walls was noted to be smaller than that of the RC slab owing to the sandwich walls absorbing more blast energy due to the deformation of MTC. The bottom steel plate of MTC could be utilized to resist the high-speed fragments generated from the top G-HPC layer. In addition, the weight of the sandwich wall was also reduced by 39% as compared to the RC slab. Comparing with the SPS-2 wall, the crater and spalling diameters of the SPS-1 wall decreased from 431.5 mm and 608 mm to 395 mm and 597.5 mm, respectively, thus, indicating that the sandwich wall with the rectangular steel tube core demonstrated a superior blast resistance than the wall with the circular steel tube core. The experimental results revealed that the fifth steel tube significantly affected the blast resistance. The reason for the observed phenomenon might be attributed to the fifth rectangular steel tube absorbing more blast energy than the fifth circular steel tube (Fig. 17 and Fig. 18 (a) and (b)). It is worth noting that the crater (431.5 mm) and spalling (608 mm) diameters of the SPS-2 wall were larger than the crater (406.5 mm) and spalling (572.5 mm) diameters of the SPSA-2 wall. This might be due to the resistance resulting from MTC of the SPSA-2 wall was inferior than that from the SPS-2 wall. The strong shock wave propagated downwards, thus, severely damaging the bottom G-HPC layer of the SPSA-2 wall. Such a severe damage consumed more blast energy and reduced its propagation, thus, leading to smaller crater and spalling diameters of the SPSA-2 wall as compared to the SPS-2 wall. The spalling damage was observed at the bottom G-HPC layer of the SPS-2 pane, while the bottom G-HPC layer of the SPSA-2 wall demonstrated the critical perforation failure, with the fracture failure appearing on the fifth aluminum alloy tube and bottom steel plate. The observed phenomena indicated that the sandwich wall with the circular steel tube core exhibited a superior blast resistance than the wall with the circular aluminum alloy tube core. This might be due to the reason that the circular steel tube absorbed more blast wave energy owing to its higher stiffness and strength as compared to the aluminum alloy tube. The deformations in the middle cross-section of the fifth circular steel tube and aluminum alloy tube are shown in Fig. 17 and Fig. 18 (b) and (c). Moreover, the fragments from the G-HPC layer were trapped by SWMs in the SPS-1 and SPS-2 walls, thus, indicating that SWM positively affected the resistance against the high-speed fragments under contact explosions.

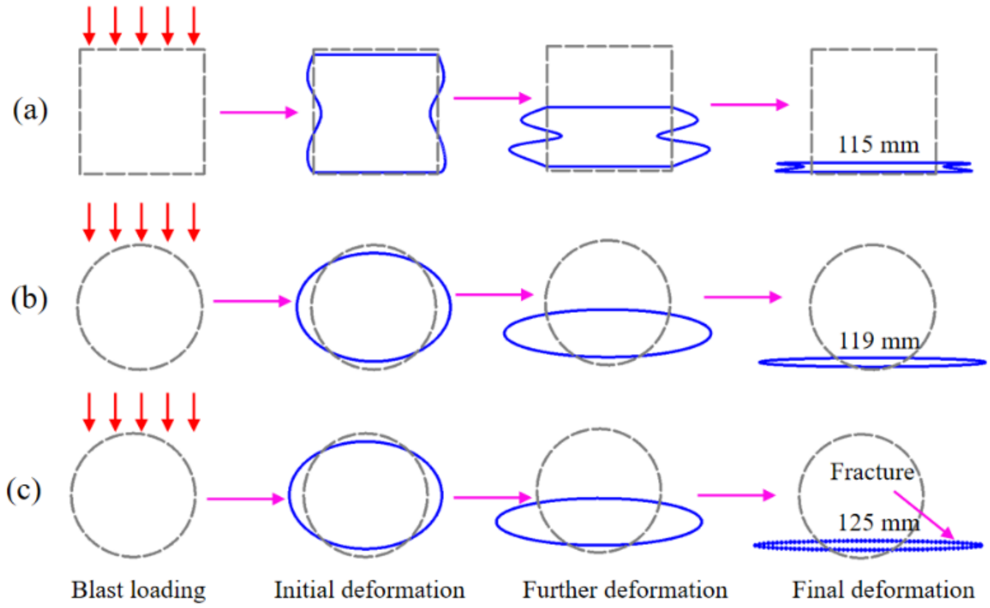

Fig. 17. The deformation schematic of the fifth metallic tube in the middle cross-section (a) rectangular steel tube, (b) circular steel tube, (c) aluminum alloy tube

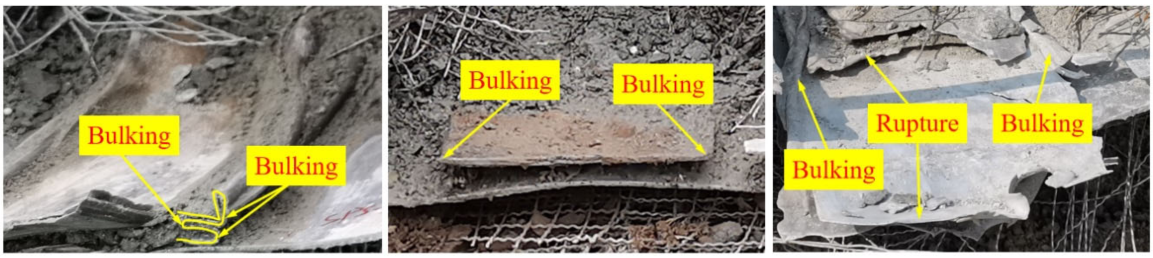

(a) rectangular steel tube (b) circular steel tube (c) circular aluminum alloy tube

Fig. 18. The deformation of the fifth metallic tube in the middle cross-section

To further illustrate that the energy absorption of the rectangular metallic tubes was superior than that of the circular metallic tubes, the lateral compression tests of the rectangular and circular steel tubes were performed. The steel tubes had a length of 80 mm. The metallic tubes were affixed on the universal testing machine and loaded at a constant velocity of 5 mm/min. The test setup and results are presented in Fig. 19 and Fig. 20, whereas the force–displacement curves are demonstrated in Fig. 21.

Fig. 19. The deformation of the rectangular steel tube

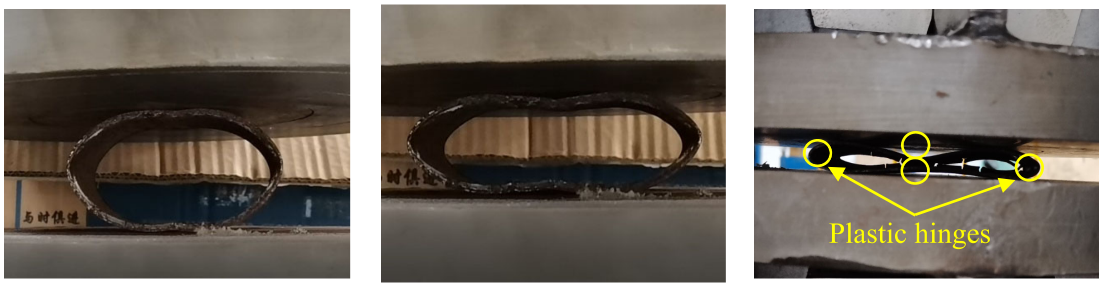

Fig. 20. The deformation of the circular steel tube

A comparison of Fig. 17 (a) and Fig. 19 indicated that the deformation of the rectangular steel tube under the quasi-static load was different from that of the sandwich wall. The observed phenomenon may be caused by the geometric imperfection and eccentric loading of the rectangular steel tube. However, the deformation of the circular steel tube under the quasi-static load was similar to that of the sandwich wall under blast loading (Fig. 17 (b) and Fig. 20). This might be due to the reason that the cross-section of the circular steel tube was much smoother as compared to the rectangular steel tube, and the influence of the geometric imperfection and eccentric loading was minimal. A comparison of Fig. 19 and Fig. 20 revealed that the rectangular steel tube could absorb more energy as compared to the circular tube, as the rectangular tube produced more plastic hinges than that of the circular steel tube. Likewise, the lateral compression force of the rectangular steel tube was larger than that of the circular steel tube, thus, further indicating that the energy absorption of the rectangular metallic tube was superior than the circular metallic tube (Fig. 21).

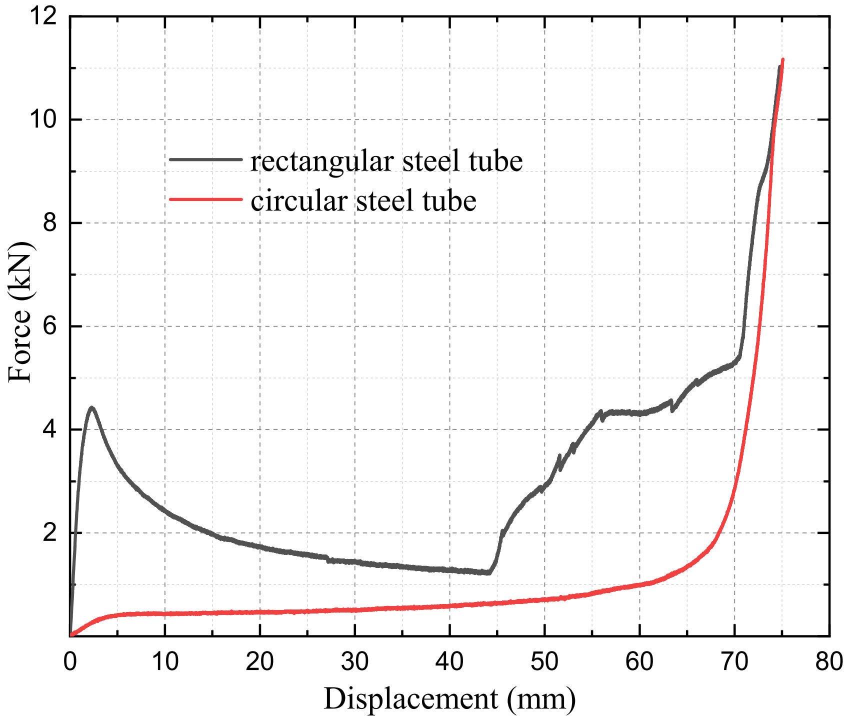

Fig. 21. The force-displacement curves of the rectangular and circular tubes

5. Failure prediction using existing methods

5.1 Analytical prediction methods

The analytical analysis of the spall damage of concrete is complex. It is affected by the shape and weight of explosives, propagation process of the stress wave, dynamic characteristics of the concrete materials, etc. In addition, there are many unknown parameters, such as the stress variation during the propagation of the blast stress wave under various working conditions. Based on different assumptions and simplifications, Kot *et al.* [41, 42] proposed an analytical analysis method for analyzing the concrete spall damage, which was suitable for the light and moderate spall damages. Remennikov *et al.* [43] proposed an analytical method to determine the breach parameters of the concrete slabs subject to contact charges. The method was used to predict the breach parameters of the high strength concrete panels, however, the applied charge mass and panel thickness limited the analysis [44].

5.2 Empirical prediction methods

In order to evaluate the failure mode of the concrete components under blast loading, many empirical methods have also been proposed in the past decades. However, the empirical methods often adopt assumptions and simplifications owing to a large number of unknown parameters, such as the variations during the construction of the concrete slabs, geometry and wave dispersion. Therefore, the available empirical methods were used to evaluate the damage in the sandwich walls subjected to blast loading, followed by the comparison of the obtained results with the experimental findings in this study. The accuracy of the empirical methods was subsequently discussed.

McVay *et al.* [45] and Morishita *et al.* [46, 47] developed an empirical formula for predicting the failure mode of the concrete slabs, which has been implemented in a number of studies [48, 49]. UFC 3-340-02 [50] provides another empirical formula for predicting the failure mode of the concrete slabs subjected to contact blast loading. In another study, Zhang *et al.* [51] proposed the spalling damage coefficient for representing the degree of damage in the concrete slabs. Wang *et al.*[52] used the empirical formula to verify its suitability for estimating the damage in the polyisocyanate-oxazodone coated square reinforced concrete slab. Thus, these empirical formulae were also used in this study to verify their suitability for predicting the damage in the sandwich walls.

McVay *et al.* [45] derived an empirical formula to evaluate the failure mode of the concrete slabs subjected to close-in blast loading based on the analysis of the 334 field test data. The scale slab thickness $T/W^{1/3}$ and scale standoff distance $R/W^{1/3}$ were proposed for predicting the damage in the concrete slab. Here, T represents the slab thickness, R is the stand-off distance, and W is the equivalent TNT mass. The threshold curves of the spalling and perforation damage proposed by McVay are plotted in Fig. 22. The sandwich walls were classified as perforation as per the damage classification system developed by McVay. The failure mode of the SPSA-2 wall was close to the

McVay's damage prediction, however, the damage evaluated by using the McVay relation was different from the damage observed for the SPS-1 and SPS-2 walls.

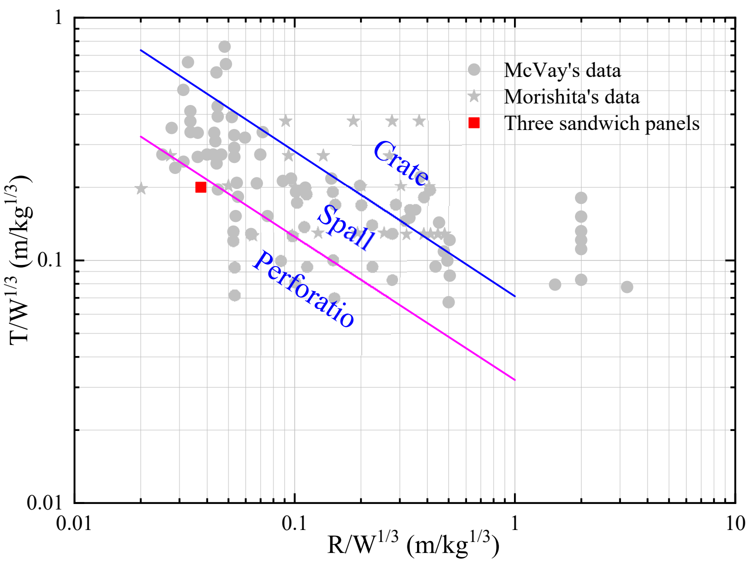

Fig. 22. The empirical evaluation proposed by McVay

Table 4 lists the empirical formulas proposed by Morishita *et al.* [46, 47], UFC 3-340-02 [50] and Zhang *et al.* [51] to predict the failure mode of the concrete slabs subjected to contact explosion. The damage prediction using the Morishita, UFC 3-340-02 and and Zhang formulae are illustrated in Fig. 24 and Fig. 24.

Table 4 Empirical formulas proposed by Morishita, UFC 3-340-02 and Zhang

Researchers	Empirical formulas	Damage prediction
Morishita *et al.* [46, 47]	Limit of crater: $T/W^{1/3} > 0.36$ Limit of crater and spalling: $0.2 < T/W^{1/3} \le 0.36$ Limit of perforation: $T/W^{1/3} \le 0.2$	Fig. 24
UFC 3-340-02 [50]	The spall threshold curve: $T/r = (a + b\psi^{2.5} + c\psi^{0.5})^{-1}$	Fig. 24

	The breach threshold curve: $T/r=(a+b\psi+c\psi^2)^{-1}$ The spall parameter (ψ) for the contact charges: $\psi=0.527r^{0.972}f_c^{0.308}W_{adj}^{-0.341}$	
Zhang *et al.* [51]	$K_Z=\dfrac{T+e}{\sqrt[3]{W}}=\begin{cases}>0.8 & crater\\ 0.25\sim0.8 & spall\\ 0.15\sim0.25 & perforation\\ <0.15 & punching\end{cases}$	Fig. 24

Note: in this table, T is the concrete thickness (ft), r is the range from the slab face to the charge center of gravity (ft), ψ is the spall parameter, and the values of the coefficients a, b and c are listed in Table 5, f_c is the compressive strength of concrete (psi), W_{adj} is the adjusted charge weight (lb), e is the height of the charge center (m).

Table 5 The coefficients of spall and breach threshold curves [50]

Coefficient	*a*	*b*	*c*
Spall threshold curve	-0.02511	0.01004	0.13613
Breach threshold curve	0.028205	0.144308	0.049265

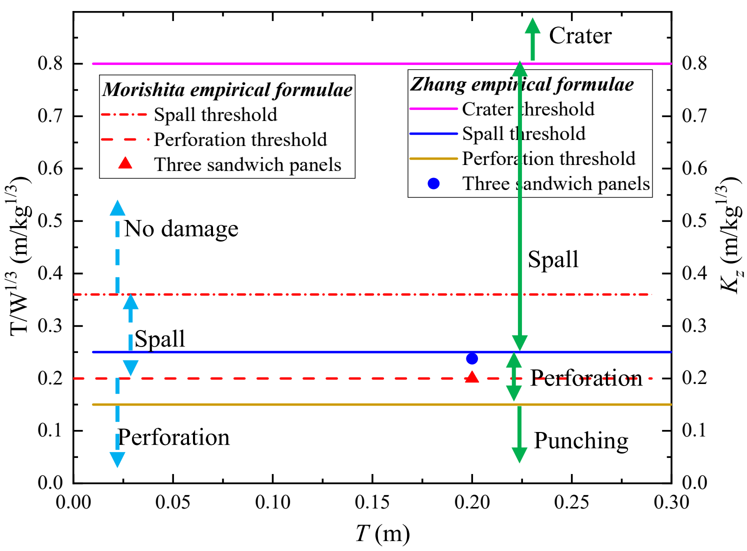

Fig. 23. The empirical evaluations proposed by Morishita [46, 47] and Zhang [51]

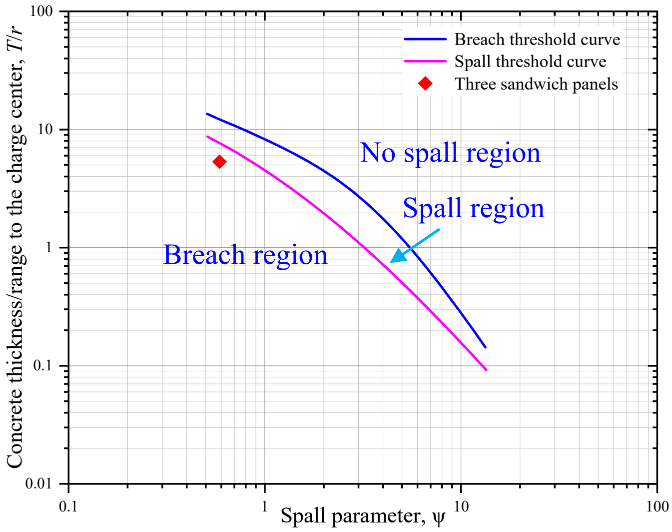

Fig. 24. The evaluation based on the UFC 3-340-02 formula

It can be seen from Fig. 24 and Fig. 24 that these formulas proposed by Morishita *et al.* [46, 47], UFC 3-340-02 [50] and Zhang *et al.* [51] could evaluate the damage of the RC slab, and they can also effectively evaluate the blast resistance of the SPSA-2 wall as the damage in the SPSA-2 wall exhibits the perforation-critical mode. However, these failed to accurately predict the failure mode of the SPS-1 and SPS-2 walls under contact explosions. This might be due to the reason that these formulae only considered slab thickness and the mass and height of TNT, however, the influence of MTC was not considered in the prediction. Thus, the damage prediction is not suitable for the SPS-1 and SPS-2 walls. In addition, as the aluminum alloy tube has inferior rigidity and strength than the steel tube, the MTC layer with the aluminum alloy tube has a smaller impact on the blast resistance capacity of the sandwich wall than the steel tube. Hence, these formulas can effectively evaluate the blast resistance of the SPSA-2 wall.

In future, more parametric studies should be carried out using the numerical tools to further analyze the damage in the sandwich walls under contact explosions. An empirical formula should be proposed to predict the failure mode of the sandwich walls by considering various factors, such as the thickness, strength and reinforcement of the top and bottom G-HPC layers as well as the height, number, type and thickness of the tubes.

6. Conclusions

In this study, the novel G-HPC sandwich walls with a metallic tube core (MTC) were developed and subsequently subjected to the 1 kg TNT contact explosions. The C40 concrete (RC) slab was also used for comparison. Based on the experimental results, the following conclusions can be drawn:

1. As compared to the RC slab, the sandwich walls exhibited a superior blast resistance, and their weight was reduced by up to 39%. MTC could be utilized to resist the high-speed fragments generated from the top G-HPC layer and absorb more blast energy owing to a large deformation.
2. The blast resistance of the sandwich wall with the rectangular steel tube core was superior than the wall with the circular steel tube core. The sandwich slab with the circular steel tube exhibited a superior blast resistance as compared with the wall with the circular aluminum alloy tube core.
3. The existing empirical models were unsuitable for accurately predicting the damage in the sandwich walls. This could be attributed to the absence of any consideration of the influence of MTC in these models.
4. SWM effectively mitigated the high-speed fragments, thereby reducing their secondary damage to the occupants in the surroundings.

Acknowledgments

The research presented herein is supported by the National Natural Science Foundation of China (Grant Nos. 51908155 and 51978186), Science and technology program of Guangzhou (Grant No. 202102020565) and the Innovation Research for the Postgraduates of Guangzhou University (Grant No. 2020GDJC-D12).

References

[1] Luccioni BM, Ambrosini RD, Danesi RF. Analysis of building collapse under blast loads. Engineering Structures. 2004;26(1):63-71.

[2] Eamon CD, Baylot JT, O'Daniel JL. Modeling concrete masonry walls subjected to explosive loads. Journal of Engineering Mechanics. 2004;130(9):1098-106.

[3] Zhao C, Ye X, He K, Gautam A. Numerical study and theoretical analysis on blast resistance of fabricated concrete slab. Journal of Building Engineering. 2020;32.

[4] Li Z, Tang D, Li W, Yan Z. Assembly blast walls and concrete blast walls comparative analysis of protective effectiveness. 3rd International Conference on Civil Engineering and Transportation (ICCET 2013). Kunming, PEOPLES R CHINA2013. p. 2355-+.

[5] Tan HWA, Chew SH, He ZW, Karunaratne GP, Seah YT. Effect of geometry & geosynthetics type on the effectiveness of reinforced soil (RS) walls as protection against blast loads. Geosynthetics, Vols 1-4. 2006:1153

[6] Scherbatiuk K, Rattanawangcharoen N. A hybrid rigid-body rotation model with sliding for calculating the response of a temporary soil-filled wall subjected to blast loading. International Journal of Impact Engineering. 2011;38(7):637-52.

[7] Hussein A, Heyliger P, Mahmoud H. Structural performance of a wood-sand-wood wall for blast protection. Engineering Structures. 2020;219.

[8] Wang JG, Ren HQ, Wu XY, Cai CL. Blast response of polymer-retrofitted masonry unit walls. Composites Part B-Engineering. 2017;128:174-81.

[9] Alsayed SH, Elsanadedy HM, Al-Zaheri ZM, Al-Salloum YA, Abbas H. Blast response of GFRP-strengthened infill masonry walls. Construction and Building Materials. 2016;115:438-51.

[10] Chen L, Fang Q, Zhang L, Zhang YD, Chen WS. Numerical investigation of a water barrier against blast loadings. Engineering Structures. 2016;111:199-216.

[11] Draganic H, Gazic G, Lukic S, Jelec M. Experimental investigation on blast load resistance of reinforced concrete slabs retrofitted with epoxy resin impregnated glass fiber textiles. Composite Structures. 2021;274.

[12] Maazoun A, Belkassem B, Reymen B, Matthys S, Vantomme J, Lecompte D. Blast response of RC slabs with externally bonded reinforcement: Experimental and analytical verification. Composite Structures. 2018;200:246-57.

[13] Wu J, Liu Z, Yu J, Xu S. Experimental and numerical investigation of normal reinforced concrete panel strengthened with polyurea under near-field explosion. Journal of Building Engineering. 2022;46.

[14] Sohel KMA, Liew JYR. Behavior of steel–concrete–steel sandwich slabs subject to impact load. Journal of Constructional Steel Research. 2014;100:163-75.

[15] Liew JYR, Wang TY. Novel steel-concrete-steel sandwich composite plates subject to impact and blast load. Advances in Structural Engineering. 2011;14(4):673-87.

[16] Remennikov AM, Kong SY. Numerical simulation and validation of impact response of axially-restrained steel-concrete-steel sandwich panels. Composite Structures. 2012;94(12):3546-55.

[17] Zhao CF, Lu X, Wang Q, Gautam A, Wang JF, Mo YL. Experimental and numerical investigation of steel-concrete (SC) slabs under contact blast loading. Engineering Structures. 2019;196.

[18] Remennikov A, Gan ECJ, Tuan N, Netherton MD. The development and ballistic performance of protective steel-concrete composite barriers against hypervelocity impacts by explosively formed projectiles. Composite Structures. 2019;207:625-44.

[19] Turner LK, Collins FG. Carbon dioxide equivalent (CO2-e) emissions: A comparison between geopolymer and OPC cement concrete. Construction and Building Materials. 2013;43:125-30.

[20] Singh B, Ishwarya G, Gupta M, Bhattacharyya SK. Geopolymer concrete: A review of some recent developments. Construction and Building Materials. 2015;85:78-90.

[21] McLellan BC, Williams RP, Lay J, van Riessen A, Corder GD. Costs and carbon emissions for geopolymer pastes in comparison to ordinary portland cement. Journal of Cleaner Production. 2011;19(9-10):1080-90.

[22] Bellum RR, Muniraj K, Indukuri CSR, Madduru SRC. Investigation on Performance Enhancement of Fly ash-GGBFS Based Graphene Geopolymer Concrete. Journal of Building Engineering. 2020;32:101659.

[23] Nuaklong P, Wongsa A, Boonserm K, Ngohpok C, Jongvivatsakul P, Sata V, Sukontasukkul P, Chindaprasirt P. Enhancement of mechanical properties of fly ash geopolymer containing fine recycled concrete aggregate with micro carbon fiber. Journal of Building Engineering. 2021;41:102403.

[24] Pawluczuk E, Kalinowska-Wichrowska K, Jiménez JR, Fernández-Rodríguez JM, Suescum-Morales D. Geopolymer concrete with treated recycled aggregates: Macro and microstructural behavior. Journal of Building Engineering. 2021;44:103317.

[25] Xu S, Yuan P, Liu J, Pan Z, Liu Z, Su Y, Li J, Wu C. Development and preliminary mix design of ultra-high-performance concrete based on geopolymer. Construction and Building Materials. 2021;308:125110.

[26] Liu J, Wu C, Li C, Dong W, Su Y, Li J, Cui N, Zeng F, Dai L, Meng Q, Pang J. Blast testing of high performance geopolymer composite walls reinforced with steel wire mesh and aluminium foam. Construction and Building Materials. 2019;197:533-47.

[27] Pasupathy K, Sanjayan J, Rajeev P, Law DW. The effect of chloride ingress in reinforced geopolymer concrete exposed in the marine environment. Journal of Building Engineering. 2021;39:102281.

[28] Pan Z, Tao Z, Cao YF, Wuhrer R, Murphy T. Compressive strength and microstructure of alkali-activated fly ash/slag binders at high temperature. Cement & Concrete Composites. 2018;86:9-18.

[29] Khan MZN, Hao Y, Hao H, Shaikh FUA, Liu K. Mechanical properties of ambient cured high-strength plain and hybrid fiber reinforced geopolymer composites from triaxial compressive tests. Construction and Building Materials. 2018;185:338-53.

[30] Al-Majidi MH, Lampropoulos A, Cundy AB. Tensile properties of a novel fibre reinforced geopolymer composite with enhanced strain hardening characteristics. Composite Structures. 2017;168:402-27.

[31] Masi G, Rickard WDA, Bignozzi MC, van Riessen A. The effect of organic and inorganic fibres on the mechanical and thermal properties of aluminate activated geopolymers. Composites Part B-Engineering. 2015;76:218-28.

[32] Meng Q, Wu C, Hao H, Li J, Wu P, Yang Y, Wang Z. Steel fibre reinforced alkali-activated geopolymer concrete slabs subjected to natural gas explosion in buried utility tunnel. Construction and Building Materials. 2020;246.

[33] Khan MZN, Hao Y, Hao H, Shaikh FUA. Mechanical properties of ambient cured high strength hybrid steel and synthetic fibers reinforced geopolymer composites. Cement and Concrete Composites. 2018;85:133-52.

[34] Li J, Wu C, Hao H, Su Y, Li Z-X. A study of concrete slabs with steel wire mesh reinforcement under close-in explosive loads. International Journal of Impact Engineering. 2017;110:242-54.

[35] Li J, Wu C, Liu Z-X. Comparative evaluation of steel wire mesh, steel fibre and high performance polyethylene fibre reinforced concrete slabs in blast tests. Thin-Walled Structures. 2018;126:117-26.

[36] GB/T3091-2015. Welded steel pipes for low pressure liquid delivery. China, 2015.

[37] GB/T6892-2015. Wrought aluminum and aluminum alloys extruded profiles for general engineering. China, 2015.

[38] GB／T3098.6-2014. Mechanical properties of fasteners-stainless steel bolts, screws and studs. China, 2014.

[39] GB/T12618.1-2006. Open end blind rivets with break pull mandrel and protruding head-property class 10, 11. China, 2006.

[40] Dua A, Braimah A. Assessment of reinforced concrete slab response to contact explosion effects. Journal of Performance of Constructed Facilities. 2020;34(4).

[41] Kot CA. Spalling of concrete walls under blast load. 4 International conference on structural mechanics in reactor technology. Commission of the European Communities (CEC);1977.

[42] Kot CA, Valentin RA, McLennan DA, Turula P. Effects of air blast on power plant structures and components (No. NUREG/CR-0442; ANL-CT-78-41). IL, USA: Argonne National Lab;1978.

[43] Remennikov A, Mentus I, Uy B. Explosive Breaching of Walls with Contact Charges: Theory and Applications. International Journal of Protective Structures. 2015;6(4):629-47.

[44] Remennikov AM, Youssef J, Ngo TD, Mentus I. Breach diameter analysis of concrete panels subjected to contact charge detonations. International Journal of Impact Engineering. 2018;120:95-109.

[45] McVay MK. Spall damage of concrete structures. ARMY Engineer Waterways Experiment Station Vicksburg MS Structures LAB; 1988.

[46] Morishita M, Tanaka H, Ito M, Yamaguchi H. Damage of reinforced concrete slabs subjected to contact detonations. Journal of Structural Engineering-Asce. 2000;46:1787-97.

[47] Morishita M, Tanaka H, Ando T, Hagiya H. Effects of concrete strength and reinforcing clear distance on the damage of reinforced concrete slabs subjected to contact detonations. Concrete Research and Technology. 2004;15(2):89-98.

[48] Tabatabaei ZS, Volz JS, Baird J, Gliha BP, Keener DI. Experimental and numerical analyses of long carbon fiber reinforced concrete panels exposed to blast loading. International Journal of Impact Engineering. 2013;57:70-80.

[49] Li Z, Liu Y, Yan J, Yu W, Huang F. Experimental investigation of p-section concrete beams under contact explosion and close-in explosion conditions. Defence Technology. 2018;14(5):540-9.

[50] Unified Facilities Criteria (UFC) 3-340-02. Structures to resist the effects of accidental explosions. Washington D.C.: U.S Department of Defense; 2008.

[51] Zhang ZY. New blasting technology in China: Metallurgical Industry Press; 2004, China.

[52] Wang W, Yang J, Wang J, Wang X, Huo Q. Experimental investigation of polyisocyanate oxazodone coated square reinforced concrete slab under contact explosions. International Journal of Impact Engineering. 2021;149.